



OPEN ACCESS

EDITED BY Maria Evelina Fantacci, University of Pisa, Italy

REVIEWED BY
Li-Sheng Geng,
Beihang University, China
Silambarasan Anbumani,
The University of Arkansas for Medical
Science, United States

*correspondence Mustafa Çağlar ☑ mcaglar@medipol.edu.tr

RECEIVED 06 August 2025

ACCEPTED 22 October 2025
PUBLISHED 13 November 2025

CITATION

Çağlar M, Ertaş KS, Cebe MS, Kara I, Kheradmand N and Metcalfe E (2025) Synthetic CT generation from CBCT using deep learning for adaptive radiotherapy in prostate cancer.

Front. Radiol. 5:1680803. doi: 10.3389/fradi.2025.1680803

COPYRIGHT

© 2025 Çağlar, Ertaş, Cebe, Kara, Kheradmand and Metcalfe. This is an open-access article distributed under the terms of the Creative Commons Attribution License (CC BY). The use, distribution or reproduction in other forums is permitted, provided the original author(s) and the copyright owner(s) are credited and that the original publication in this journal is cited, in accordance with accepted academic practice. No use, distribution or reproduction is permitted which does not comply with these terms.

Synthetic CT generation from CBCT using deep learning for adaptive radiotherapy in prostate cancer

Mustafa Çağlar^{1*}, Kerime Selin Ertaş^{1,2}, Mehmet Sıddık Cebe³, Ilkay Kara^{1,4}, Navid Kheradmand^{1,4} and Evrim Metcalfe^{2,5}

¹Department of Health Physics, Graduate School of Health Sciences, İstanbul Medipol University, İstanbul, Türkiye, ²Department of Radiation Oncology, Medipol Bahçelievler Hospital, İstanbul, Türkiye, ³Program of Radiotherapy, Vocational School, İstanbul Medipol University, İstanbul, Türkiye, ⁴Program of Radiotherapy, Vocational School and Health Services, İstanbul Medipol University, İstanbul, Türkiye, ⁵Department of Radiation Oncology, School of Medicine, İstanbul Medipol University, İstanbul, Türkiye

Objective: In this study, the accuracy of deep learning-based models developed for synthetic CT (sCT) generation from conventional Cone Beam Computed Tomography (CBCT) images of prostate cancer patients was evaluated. The clinical applicability of these sCTs in treatment planning and their potential to support adaptive radiotherapy decision-making were also investigated.

Methods: A total of 50 CBCT-CT mappings were obtained for each of 10 retrospectively selected prostate cancer patients, including one planning CT (pCT) and five CBCT scans taken on different days during the treatment process. All images were preprocessed, anatomically matched and used as input to the U-Net and ResU-Net models trained with PyTorch after z-score normalisation. The sCT outputs obtained from model outputs were quantitatively compared with the pCT with metrics such as SSIM, PSNR, MAE, and HU difference distribution.

Results: Both models produced sCT images with higher similarity to pCT compared to CBCT images. The mean SSIM value was 0.763 ± 0.040 for CBCT-CT matches, 0.840 ± 0.026 with U-Net and 0.851 ± 0.026 with ResU-Net, with a significant increase in both models (p < 0.05). PSNR values were 21.55 ± 1.38 dB for CBCT, 24.74 ± 1.83 dB for U-Net, and 25.24 ± 1.61 dB for ResU-Net. ResU-Net provided a statistically significant higher PSNR value compared to U-Net (p < 0.05). In terms of MAE, while the mean error in CBCT-CT matches was 75.2 ± 18.7 HU, the U-Net model reduced this value to 65.3 ± 14.8 HU and ResU-Net to 61.8 + 13.7 HU (p < 0.05).

Conclusion: Deep learning models trained with simple architectures such as U-Net and ResU-Net provide effective and feasible solutions for the generation of clinically relevant sCT from CBCT images, supporting accurate dose calculation and facilitating adaptive radiotherapy workflows in prostate cancer management.

KEYWORDS

synthetic CT, CBCT, deep learning, image-guided radiotherapy (IGRT), adaptive radiotherapy

1 Introduction

Radiotherapy is a major component of cancer treatment and is applied in more than 50% of patients, either alone or in combination with surgery and systemic therapies. It aims to deliver radiation to the tumor site with high precision while minimizing damage to healthy tissues. Achieving this precision is critical for increasing the tumor control probability while reducing the normal tissue complication probability. Maintaining this balance in radiotherapy depends on several factors. Accurate delineation of target volumes and OARs is the primary factor in achieving effective and safe radiotherapy. Traditionally, computed tomography (CT) simulation has been considered the gold standard for this purpose (1). Another important factor is the accuracy of the patient's spatial position at the time of treatment. This accuracy is currently achieved by various Image Guided Radiotherapy (IGRT) methods. While kV portal imaging offers two-dimensional matching with digital reconstructed radiography (DRR) images obtained from CT, cone beam computed tomography (CBCT) provides volumetric imaging, enabling the monitoring of anatomical changes and treatment adaptation (2).

Soft tissue-based IGRT has replaced two-dimensional (2D) correction methods (3, 4). Among these online position correction methods, CBCT is the fastest and most accessible for conventional C-Arm and O-Ring linac systems (5). Thus, CBCT has become an indispensable component of patient positioning and daily treatment verification processes in radiotherapy clinics (1). The main advantage of CBCT compared to conventional CT is that it can be obtained on the treatment table and thus can respond immediately to anatomical changes. In this context, CBCT also forms the basis of adaptive radiotherapy (ART) applications (6). However, CBCT images are characterized by serious artifacts, low contrast resolution and most importantly inaccurate HU (Hounsfield Unit) values compared to conventional CT due to their low dose acquisition and differences in imaging geometries (7). These limitations seriously limit the use of CBCT in direct dose calculations and intensity-based segmentation/planning algorithms. In particular, failure to provide HU accuracy causes errors in dose distribution in photon/electron planning, while in sensitive modalities such as proton, even a few HU deviations can lead to deviations with intervals of a few millimeters (8, 9).

In order to improve the CBCT image quality, many methods have been proposed in the past (10–12). Among the hardware solutions, anti-scatter grid placement, ray blocking patterns or lead cages are noteworthy (13). Software solutions include methods such as iterative reconstruction (IR), ray tracing, model-based corrections and Monte Carlo (MC)-based simulations. Although MC-based approaches in particular provide successful results in terms of HU accuracy, they have not been put into clinical practice due to their high computational load (14).

The sCT generation has been proposed as an effective solution to resolve these challenges (10). This process involves the generation of CT-like images using various techniques such as bulk density assignment, atlas-based methods, hybrid methods, and deep learning-based approaches. Among these techniques, deep learning-based methods have proven to be the most the

most promising approach (10, 15–18). In particular, direct sCT generation from CBCT images has become possible by using convolutional neural networks (CNN). Thus, the strategies used for CT generation from MRI have begun to be used in CBCT transformation as well as in low-dose CT enhancements (17, 19). Ryu et al. took these approaches a step further and proposed a new architecture called COMPUNet, which includes both multi-planar and 2.5D data approaches to improve CBCT quality. This model enhances learning efficiency, even when data availability is limited, and remains robust to slight spatial misalignments between input and output images. In addition, a contextual loss term is integrated in addition to the traditional L1 loss function. Thus, artifacts are attenuated while preserving details, and clinically significant improvements are achieved (20).

Zhang et al. presented one of the important studies in this field, generating images with CT-like appearance from pelvic CBCT images using a model based on the 2.5D Pix2pix GAN architecture. The model was strengthened with additional learning criteria such as feature matching and perceptual loss, and compared with different architectures (U-Net, CycleGAN). The results demonstrated that the MAE value was reduced to around 8 HU with the 2.5D GAN architecture, and the PSNR value reached 24 (21). Moreover, Kida et al. studied sCT generation from pelvic region CBCT with U-Net and reduced the MAE value from 92 to 31 HU (22). Zhu et al. introduced a residual block-based three-dimensional (3D) U-Net architecture combined with Dice-Focal loss to facilitate efficient, fully automated segmentation of head and neck anatomy (23). Liu et al. implemented a deep attention-based CycleGAN model in their study and achieved a reduction in MAE from 81 HU to 57 HU for the abdominal region (24).

Although GAN-based models can achieve high accuracy, they generally require larger datasets, longer training times, and greater computational resources, which can limit their clinical feasibility (15, 24, 25). Beyond CNN-based methods, diffusion models have been explored for CBCT-to-CT synthesis, reporting improved artifact suppression and high-frequency detail preservation (26–28). In parallel, transformer-based architectures, including Swin variants and hybrid CNN-transformer models, have been investigated for CBCT correction and sCT generation, leveraging long-range dependencies to enhance global consistency (29–31). These advanced approaches demonstrate strong performance but typically demand substantial data and computational resources, which may hinder their translation in resource-constrained clinical settings.

In this study, we focus on lightweight, relatively simple and resource-efficient CNN architectures, specifically U-Net and ResU-Net, as practical alternatives for prostate CBCT-to-sCT generation. These models are relatively simple, stable, and reproducible, making them more suitable for limited-data environments. Our contribution lies in demonstrating feasibility in a pilot study with multi-temporal CBCT data, where "multi-temporal" refers to multiple CBCT acquisitions obtained from the same patient across different treatment fractions (different days), from real patient treatments, emphasizing the clinical practicality of lightweight models under resource constraints.

With this approach, we aim to show that deep learning models built on simpler architectures can still provide clinically relevant results and form a foundation for future integration into adaptive radiotherapy workflows.

2 Methods

2.1 Patient selection and imaging protocol

In this retrospective study, 10 patients diagnosed with prostate adenocarcinoma were randomly selected from the institutional radiotherapy archive and treated at the Radiation Oncology Department of Bahçelievler Medipol Hospital between 2019 and 2024. For each patient, one conventional planning CT scan and five separate CBCT images acquired on different days during the treatment course were included in the analysis. A total of 50 paired CBCT-CT image sets were generated. All image data were acquired in anonymized DICOM format and analyzed in accordance with the exemption granted by the local ethics committee (Non-Interventional Clinical Research Ethics Committee, Verification Code: 365043D5X6).

Planning CT images were acquired using a Siemens Biograph mCT 40 (Siemens Healthineers, Erlangen, Germany) scanner with a tube voltage of 120 kVp and a dose parameter of 132 mAs, resulting in voxel dimensions of $1.5\times1.5\times2$ mm³. CBCT images were acquired using a Halcyon linear accelerator (Varian Medical Systems, Palo Alto, CA, USA) with a voxel size of $0.96\times0.96\times1.25$ mm³ and a matrix size of $512\times512\times120$. All images were registered for each patient, and CBCT scans were selected from different treatment fractions to ensure optimal anatomical consistency with the corresponding pCT.

2.2 Image preprocessing and slice matching

CBCT and CT datasets were imported and processed from DICOM format using the *SimpleITK* library within a Python 3.9 environment. To ensure spatial consistency, CBCT volumes were resampled to match the resolution of the corresponding planning CT scans, standardizing voxel dimensions across all datasets. A linear interpolation method was applied during the resampling process.

Each CBCT dataset was rigidly registered to the corresponding planning CT scan. Slice-wise alignment was then performed, and slices lying outside the overlapping anatomical region between CBCT and CT were excluded. In addition, slice correspondence was visually verified by a radiation oncologist and a medical physicist to ensure that key pelvic structures (e.g., prostate, rectum, bladder, femoral heads) were adequately represented. Slices showing severe mismatch due to differences in bladder/rectum filling or patient positioning were also discarded. After this process, a total of 1,890 slice pairs were retained, of which 1,323 were used for training, 283 for validation, and 284 for testing at the patient level.

This step was intended to isolate differences in image quality while minimizing the impact of anatomical variability. The alignment process was conducted individually for each patient, and only overlapping anatomical regions were used for model training. All images were normalized based on HU values using z-score normalization (mean = 0, std = 1) to standardize the input for model training. The normalized datasets were then converted to. npy format and used as input for the training process.

2.3 Deep learning architectures

This study employed two distinct fully convolutional neural network architectures for image translation. Each convolutional block consisted of two 3×3 convolutions with batch normalization and ReLU activation. In ResU-Net, identity skip connections were added to each block to stabilize training. Residual blocks enhanced feature extraction without a significant increase in parameters.

2.3.1 U-Net

The U-Net architecture adopts the classical encoder–decoder design originally introduced by Ronneberger et al. 2D CBCT slice (256×256) is progressively downsampled in the encoder path through four convolutional blocks (channels: $32\to64\to128\to256\to512$), each block containing 3×3 convolutions, batch normalization, ReLU activation, and max pooling (32). The bottleneck layer consisted of 1,024 filters with a dropout rate of 0.5. The decoder path symmetrically upsamples the feature maps (channels: $512\to256\to128\to64\to32$) using 2×2 upconvolutions, concatenation with encoder features via skip connections, and subsequent convolutional blocks. This design preserves both global and local contextual information during reconstruction of the synthetic CT output.

2.3.2 ResU-Net

ResU-Net incorporates residual connections (identity mappings) into each convolutional block of the original U-Net architecture. The encoder follows the same progression of channels (32 \rightarrow 64 \rightarrow 128 \rightarrow 256 \rightarrow 512), with each block implemented as a residual block to enhance gradient flow and training stability. The bottleneck consisted of 1,024 filters with dropout (0.5) and residual blocks. The decoder similarly performs upsampling (channels: 512 \rightarrow 256 \rightarrow 128 \rightarrow 64 \rightarrow 32) using 2×2 up-convolutions followed by residual blocks. This integration mitigates the vanishing gradient problem and allows for deeper feature extraction without a significant increase in model complexity.

All model architectures were implemented from scratch in Python using the PyTorch 1.13.1 framework. Model training was conducted locally on a dedicated workstation featuring an NVIDIA GeForce GTX 1660 GPU (NVIDIA Corporation, Santa Clara, CA) with 6 GB of memory.

2.4 Training protocol

The model was trained on a slice-wise basis. One-to-one correspondence between CBCT and CT slices was ensured for

each mapping. Both models were trained using a combined L1 and mean squared error (MSE) loss function, chosen to balance structural preservation with HU fidelity. Models were trained for 200 epochs with a batch size of 1 using the Adam optimizer (learning rate 1×10^{-4} , $\beta 1=0.9$, $\beta 2=0.999$). Early stopping with a patience of 20 epochs was employed to prevent overfitting. Data augmentation included random horizontal/vertical flips and rotations within $\pm 10^\circ$. Data were normalized to [0,1], and all images were resampled to a uniform voxel spacing of $1\times 1\times 1$ mm³ prior to training. Training and validation data were split using slice-level randomization, with 80% allocated

TABLE 1 Mean \pm standard deviation values of all evaluation metrics and statistical significance comparisons for CBCT–CT, U-Net sCT–CT, and resU-Net sCT–CT matches (n=50 matched pairs; significance level set at p<0.05).

| Metric | CBCT- CT | U-Net sCT- CT | ResU-Net sCT-CT | p-value |
|--------------|-------------------|-------------------|--------------------|---------|
| SSIM | 0.763 ± 0.040 | 0.840 ± 0.026 | 0.851 ± 0.026 | a, b |
| PSNR (dB) | 21.55 ± 1.38 | 24.74 ± 1.83 | 25.24 ± 1.61 | a, b, c |
| MAE (HU) | 75.2 ± 18.7 | 65.3 ± 14.8 | 61.8 ± 13.7 | a, b, c |

p < 0.05 was considered statistically significant. a Significant difference between CBCT–CT and U-Net sCT–CT. b Significant difference between CBCT–CT and ResU-Net sCT–CT. c Significant difference between U-Net sCT–CT and ResU-Net sCT–CT.

for training and 20% for validation. The schematic diagrams of the U-Net and ResU-Net architectures are provided in Supplementary Figures S1a,b, respectively.

2.5 Performance evaluation metrics

The outputs of the model, sCT images, were compared with the reference pCT and evaluated using several quantitative metrics. These included Structural Similarity Index (SSIM), measuring structural resemblance; Peak Signal-to-Noise Ratio (PSNR), Mean Absolute Error (MAE), representing the average HU difference; and the histogram of direct HU differences. Statistical analyses were performed using two-tailed Student's t-test, with p < 0.05 considered statistically significant. The performance of U-Net and ResU-Net models was analyzed individually for each metric, and improvements over the original CBCT images were quantitatively demonstrated.

3 Results

In this study, the effectiveness of U-Net and ResU-Net architectures was evaluated for generating sCT images from

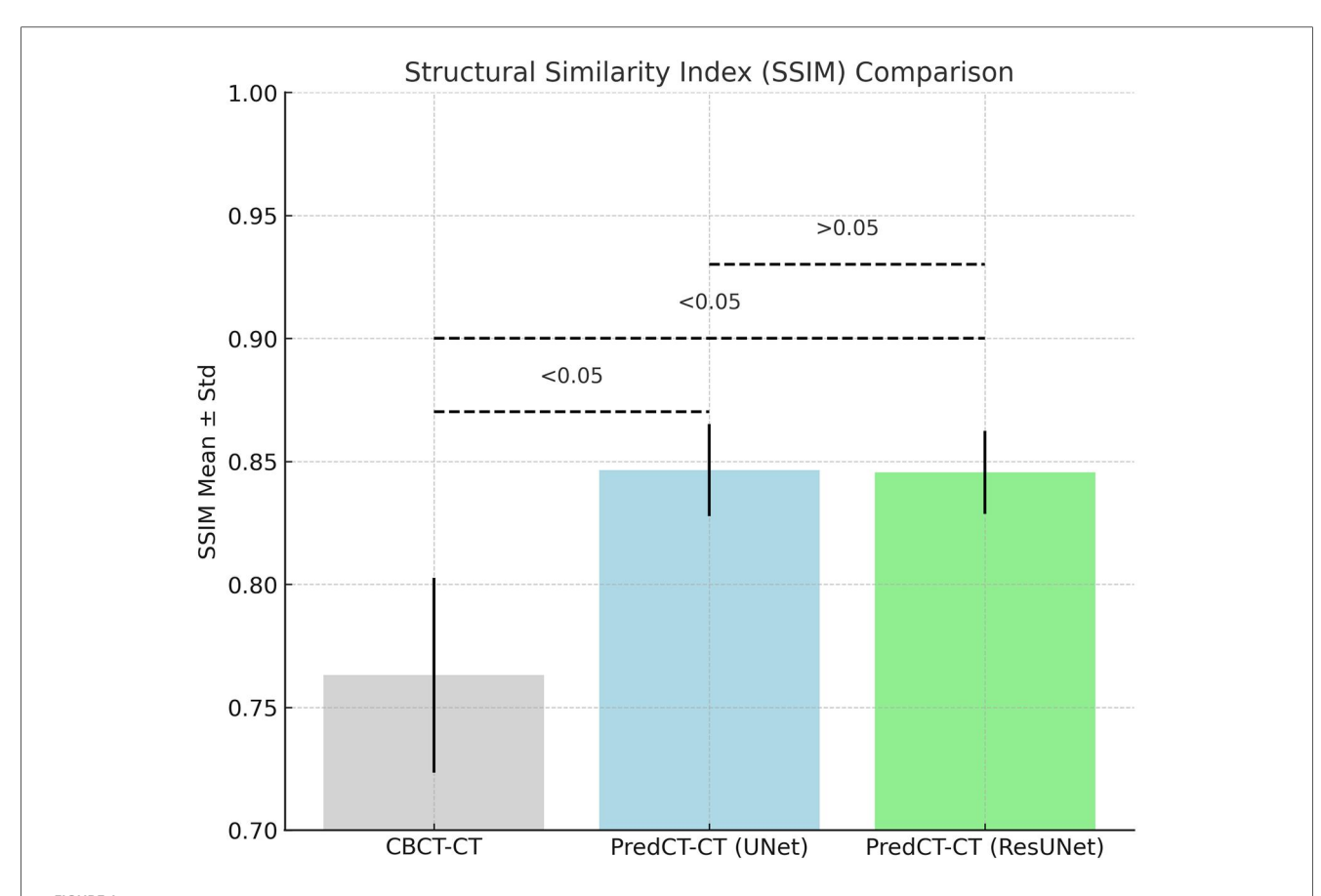


FIGURE 1
Comparison of SSIM values for CBCT-pCT, U-Net-based sCT-pCT, and resU-Net-based sCT-pCT pairs, presented as mean \pm standard deviation Statistically significant differences between groups (p < 0.05) are indicated on the plot.

CBCT scans, aiming to achieve image quality comparable to pCT. Following the training and testing of the models on 50 CBCT-CT image pairs obtained from 10 patients, the resulting sCT images were quantitatively compared to the corresponding reference CT using a set of established image quality metrics.

3.1 Quantitative evaluation

Both models generated sCT outputs that demonstrated improved similarity to the reference CT images compared to the original CBCT scans. Comparative analyses were performed for both CBCT–CT and sCT–pCT pairs produced using the U-Net and ResU-Net architectures. Evaluation metrics included SSIM, PSNR, MAE, and average HU difference. The mean and standard deviation values for each metric, along with statistical comparisons for significance, are summarized in Table 1.

According to Figure 1, both models significantly improved SSIM scores compared to the CBCT images (p < 0.05). While the mean SSIM was 0.763 ± 0.040 for CBCT-CT pairs, it increased to 0.840 ± 0.026 for U-Net sCT-CT and 0.851 ± 0.026 for ResU-Net sCT-CT. Statistical analysis confirmed that both U-Net and ResU-Net provided significant enhancements over

CBCT; however, the difference between U-Net and ResU-Net was not statistically significant (p > 0.05).

As shown in Figure 2, the mean PSNR for CBCT–CT pairs was 21.55 ± 1.38 dB, while U-Net sCT–CT and ResU-Net sCT–CT yielded 24.74 ± 1.83 dB and 25.24 ± 1.61 dB, respectively. Both models demonstrated significantly higher PSNR values compared to CBCT (p < 0.05). Moreover, the ResU-Net model significantly outperformed U-Net in terms of PSNR (p < 0.05).

The mean HU difference for CBCT–CT pairs was 75.2 ± 18.7 HU. This was reduced to 65.3 ± 14.8 HU with U-Net and further to 61.8 ± 13.7 HU using ResU-Net (Figure 3). Both models showed significant improvements in HU accuracy over CBCT (p < 0.05), while ResU-Net also demonstrated a statistically significant advantage over U-Net (p < 0.05). Likewise, the MAE was 74.4 ± 36.8 HU on average in CBCT–CT, was reduced to 64.8 ± 29.6 HU with U-Net, and further decreased to 62.1 ± 30.0 HU with ResU-Net (Figure 4).

Based on these findings, although both models effectively improved the similarity of CBCT images to the pCT, the ResU-Net architecture achieved superior performance particularly in terms of structural similarity and reduction of reconstruction errors.

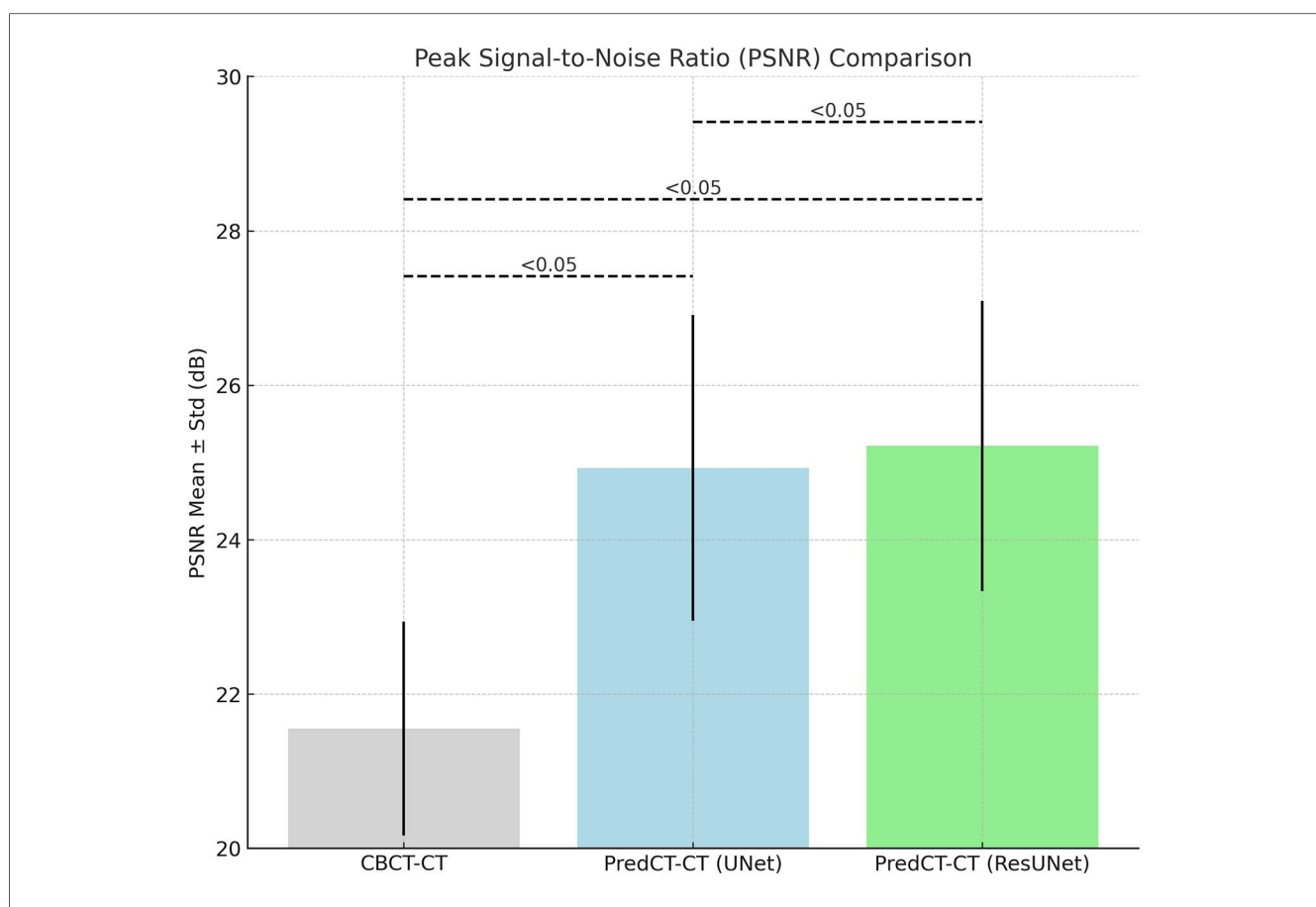
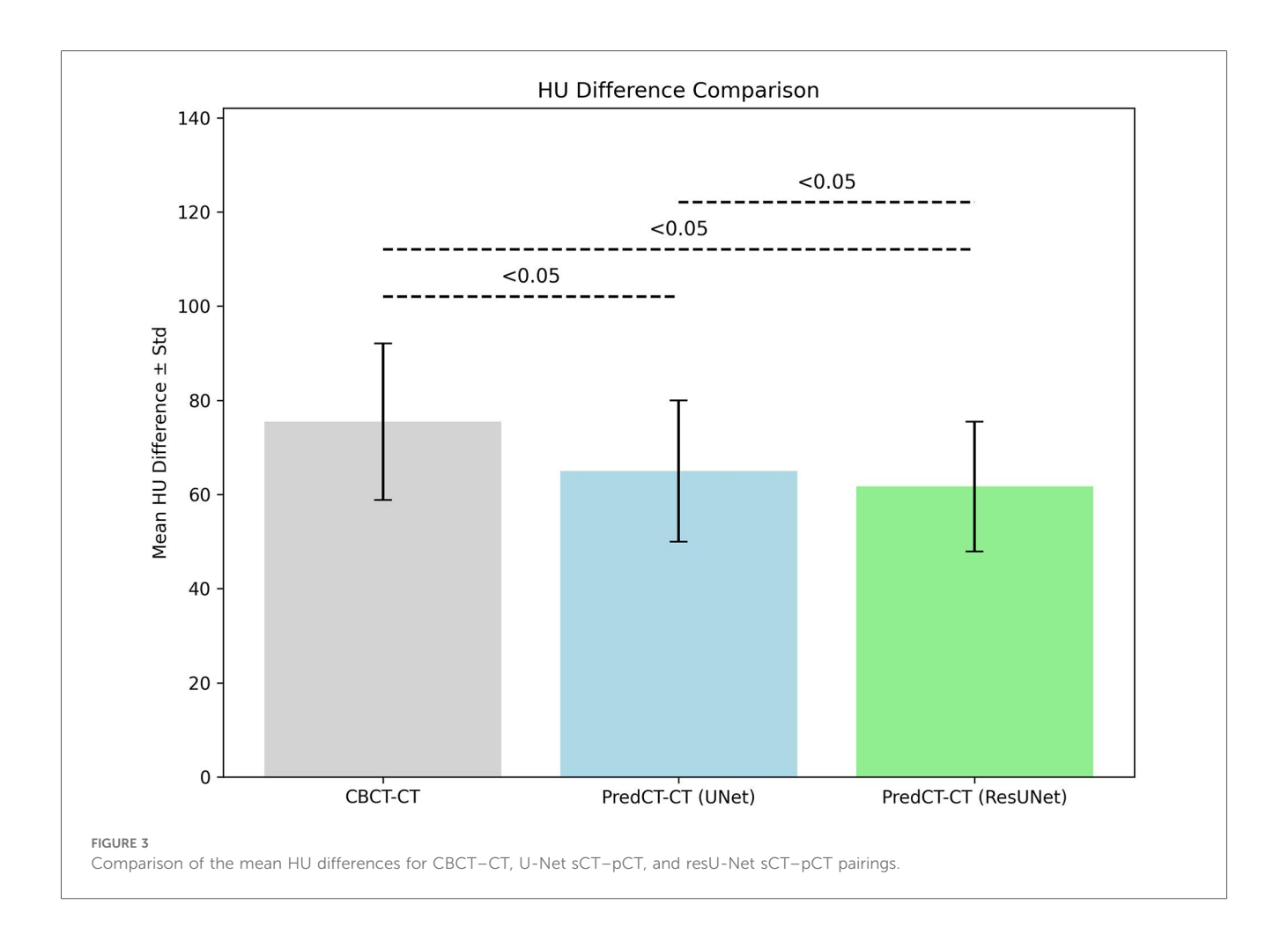


FIGURE 2

Comparison of PSNR (peak signal-to-noise ratio) values for CBCT-CT, U-Net-based sCT-CT, and resU-Net-based sCT-CT pairs, presented as mean ± standard deviation.



3.2 Qualitative evaluation

However, evaluating model performance requires not only analyzing mean HU differences but also examining their distributional characteristics. For this purpose, HU difference boxplots were generated, summarizing the central tendency, range, and outliers for all test cases (Figure 5a). The results demonstrate that raw CBCT images exhibit large deviations and outliers, particularly toward the negative HU range. While the U-Net model was able to reduce the spread of HU differences, the ResU-Net architecture produced even tighter distributions, reflecting improved robustness and consistency across patients.

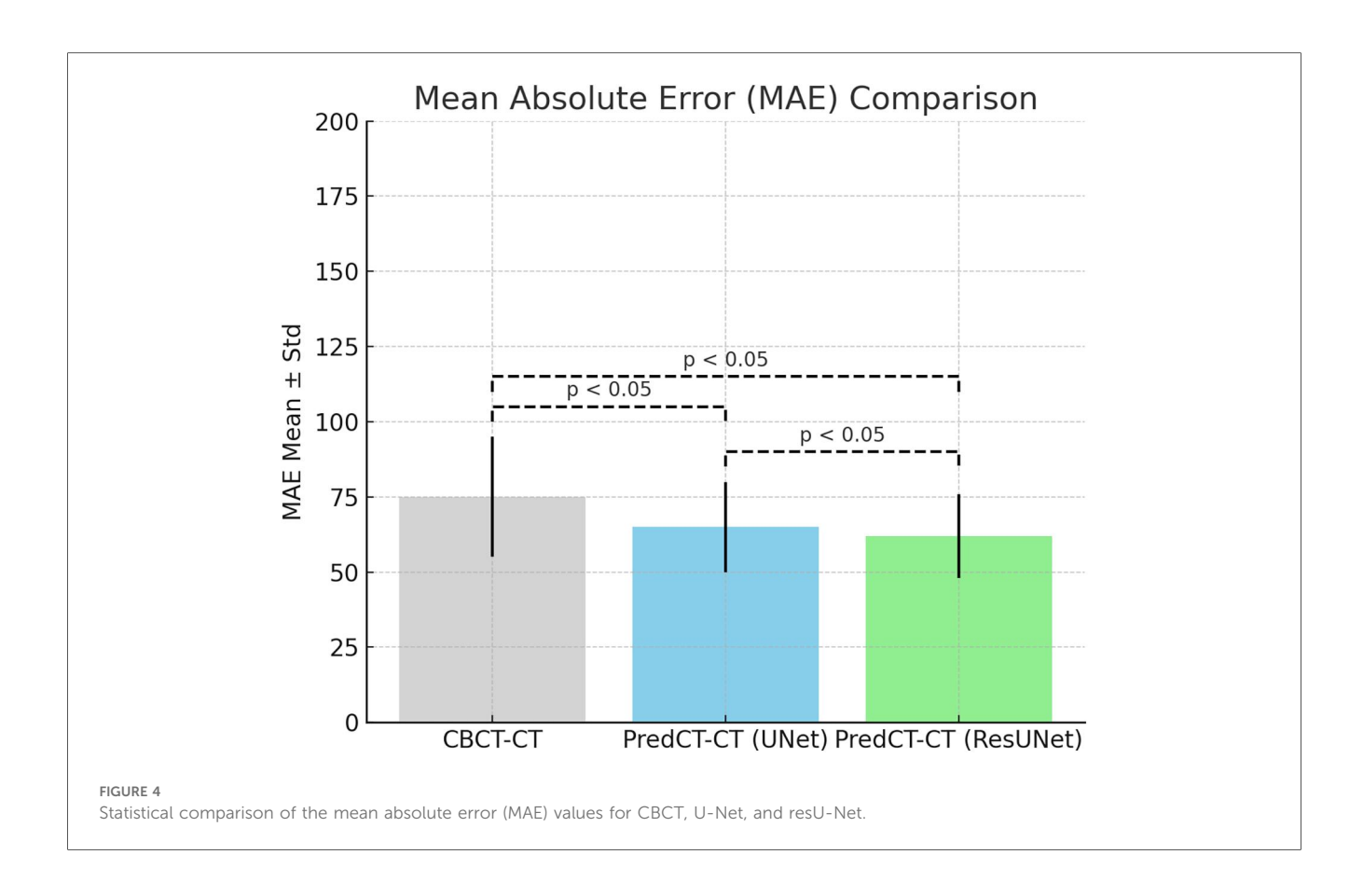
Figure 5b displays the mid-slice of CBCT10.1 (patient 10, fraction 1) the planning CT, the raw CBCT, and the synthetic CT images generated by U-Net and ResU-Net, enabling a direct qualitative comparison of anatomical structures and visual fidelity across modalities. Figure 5c presents the mid-slice difference maps that visually reflect the anatomical alignment indicated by the quantitative analyses. In the CBCT map, pronounced deviations are visible, particularly at bone-to-soft tissue boundaries. While the U-Net model managed to reduce these discrepancies to a certain extent, ResU-Net achieved a more even correction of HU values and produced outputs that more closely resembled the reference CT. When considered alongside the numerical results, these visual

observations reinforce the overall impression that ResU-Net provides a more consistent and dependable representation of HU information.

4 Discussion

In this study, the performance of the deep learning based model developed to generate sCT from conventional CBCT images was evaluated with quantitative metrics such as SSIM, PSNR, MAE, and HU. The results show that the closeness of the generated sCT images to the original CT images is significantly increased compared to the raw CBCT images.

The SSIM analysis demonstrated that both U-Net and ResU-Net architectures more effectively preserved structural information compared to conventional CBCT. The mean SSIM value for CBCT-CT alignment was 0.76, whereas it improved to 0.84 with U-Net and 0.85 with ResU-Net. These improvements were statistically significant when compared to CBCT. However, the slight advantage of ResU-Net over U-Net did not reach statistical significance. Although the SSIM values reported here are lower than the 0.93–0.98 range achieved by GAN-based models as described by Maspero et al., the results remain clinically acceptable given the model's simplicity and the limited dataset used (33).

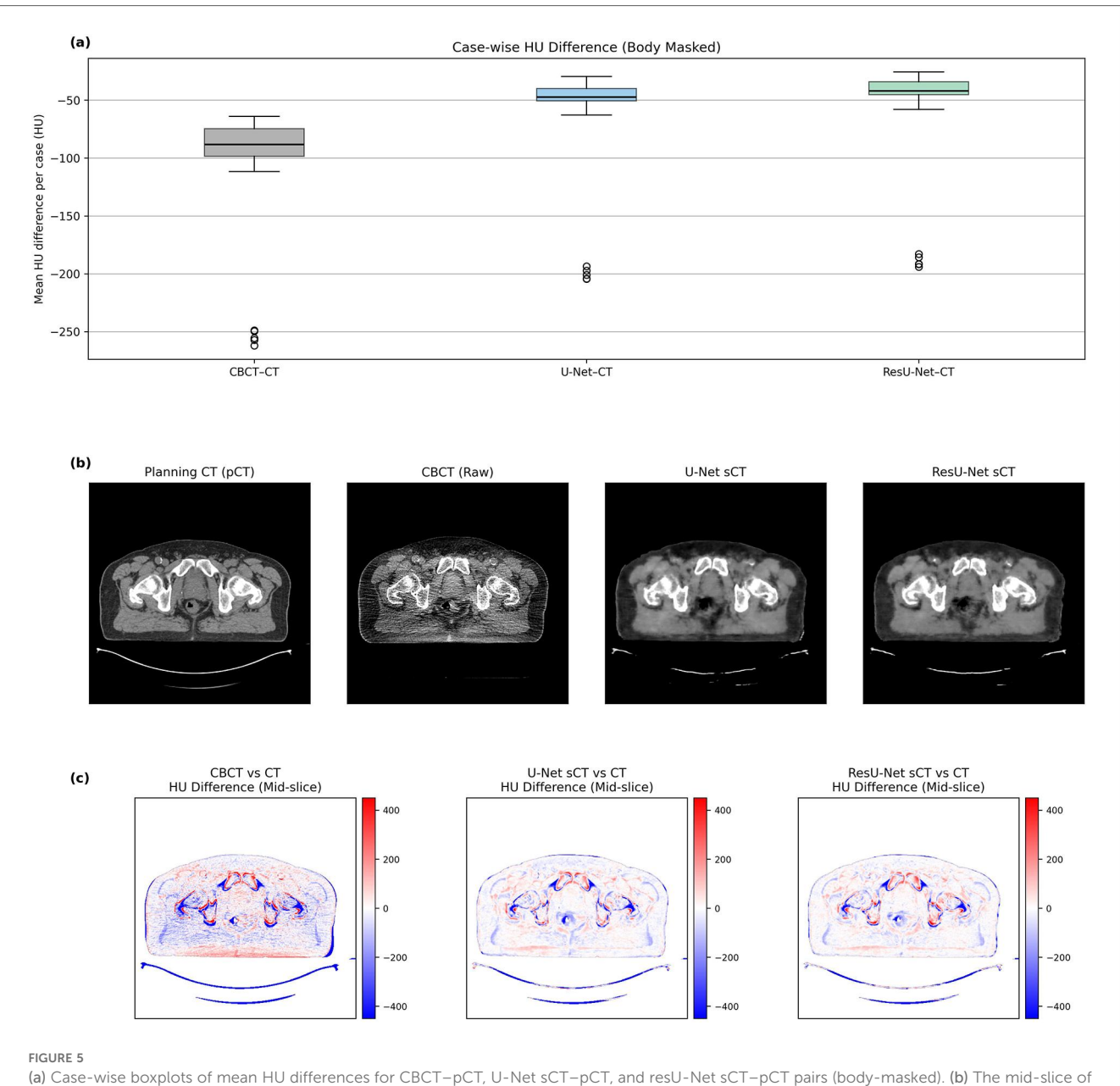


The PSNR metric was employed to assess the signal fidelity of the generated sCT images. The average PSNR, calculated as 21.55 dB for CBCT–CT comparisons, increased to 24.74 dB with U-Net and 25.24 dB with ResU-Net. Both models yielded statistically significant improvements compared to CBCT, and ResU-Net demonstrated a notably higher PSNR than U-Net (p < 0.05). This result indicates that ResU-Net enhances sCT quality by more effectively preserving anatomical structures. The obtained values are consistent with the acceptable PSNR range for sCT quality, reported in the literature to be between 25 and 28 dB (17, 34).

A similar pattern was observed in the MAE results. The average MAE for CBCT-CT alignment was measured at 75.2 HU, which decreased to 64.1 HU with U-Net and 61.8 HU with ResU-Net. Both deep learning models achieved statistically significant reductions in error compared to CBCT (p < 0.05). Furthermore, ResU-Net demonstrated a modest yet statistically significant advantage over U-Net, indicating that residual connections enhance the suppression of HU-related discrepancies. In previous research, Wongtrakool et al. reported reducing the mean MAE to approximately 58 HU using a GAN-based approach in the head and neck region (17). While the MAE values obtained in our study are slightly higher than those reported in some previous study and commercial implementations, they nevertheless highlight the feasibility of lightweight CNN architectures in improving CBCT image quality. These findings should be interpreted as proof-ofconcept results, with further optimization and larger datasets required to establish clinical acceptability. Despite its simpler architecture, the ResU-Net model employed in this study achieved comparably low MAE values, underscoring its potential to balance algorithmic efficiency with clinical relevance.

Figure 5 presents case-wise HU difference boxplots and mid-slice difference maps that visually support the quantitative findings. The boxplot analysis reveals that CBCT images exhibit a broad distribution with pronounced variability and outliers, whereas the U-Net model reduces this spread and the ResU-Net architecture further centralizes the HU values, indicating improved accuracy and consistency across patients. Similarly, mid-slice difference maps indicate prominent deviations at bone-soft tissue interfaces in CBCT images, whereas ResU-Net suppresses these discrepancies more uniformly, yielding an image that closely aligns with the pCT. Further inspection revealed that the outlier points in Figure 5A predominantly originated from high-density bony regions and adjacent interfaces, where inherent HU gradients and CBCTspecific artifacts such as scatter and beam hardening cause local intensity deviations. Despite these localized discrepancies, the synthetic CTs exhibited consistent HU improvement over raw CBCT, particularly at bone-soft tissue boundaries, as also evident in Figure 5C. When considered collectively, these findings suggest that the ResU-Net architecture provides more stable and reliable performance in terms of HU accuracy, both in pixel differences and mean absolute error.

Although simpler than GAN-based models, the U-Net and ResU-Net architectures implemented in this study achieved performance levels consistent with previous research and suitable



(a) Case-wise boxplots of mean HU differences for CBCT-pCT, U-Net sCT-pCT, and resU-Net sCT-pCT pairs (body-masked). (b) The mid-slice of CBCT10.1 (patient 10, fraction 1), including the planning CT, the raw CBCT, and the synthetic CT images generated by U-Net and ResU-Net, enabling a direct qualitative comparison of anatomical structures and visual fidelity across modalities. (c) Corresponding HU difference maps of CBCT, U-Net sCT, and ResU-Net sCT relative to the reference planning CT in the same mid-slice.

for feasibility assessment in clinical imaging quality improvement. For instance, the cGAN model used by O'Connor et al. for MR-based sCT generation demonstrated high SSIM scores and low HU deviations, but required a more complex and data-intensive training process (10). In contrast, the ResU-Net model, enhanced with residual connections, produced comparable results in both HU accuracy and structural similarity while preserving a relatively simple design.

In this context, the approaches introduced in this study offer alternative model architectures that are effective under limited data conditions and hold strong potential for clinical integration. Given that only 10 patients (50 paired CBCT-CT volumes) were included, the findings should be interpreted as a pilot feasibility

study rather than a robust validation. We also acknowledge that the feasibility of deep learning-based CBCT enhancement has been demonstrated in earlier studies; however, our contribution emphasizes the applicability of lightweight architectures in prostate cancer and multi-temporal CBCT settings, highlighting a practical pathway under resource-constrained clinical conditions.

Another notable limitation is that the study was conducted using 2D slice-based architecture. In addition, although both U-Net and ResU-Net significantly reduced the MAE compared to CBCT, the absolute values remained modest and slightly higher than those reported in some previous studies and commercial systems, indicating that further optimization is needed before clinical acceptability can be established. Future

research should therefore explore more advanced approaches, including three-dimensional CNNs, and incorporate larger, multi-center datasets to enhance model generalizability. Moreover, comprehensive evaluations are needed, including integration into clinical workflows, assessment of dose calculation accuracy, auto-contouring performance, and DVH integrity. Therefore, the present results should be interpreted as a feasibility study at the imaging quality level only, while future work must establish true clinical utility for radiotherapy applications.

5 Conclusion

These findings that deep suggest learning-based transformation methods, even those employing relatively simple architectures, can be effectively applied in clinical settings with limited data availability. The results indicate that U-Net, and especially ResU-Net, enhance CBCT image quality and enable reliable sCT generation, providing proof-of-concept feasibility in a pilot setting. This study highlights the clinical practicality of lightweight CNN architectures for sCT generation in prostate radiotherapy. Nevertheless, further validation with larger multiinstitutional datasets and advanced methods is warranted. In particular, comprehensive evaluations such as dosimetric accuracy, auto-contouring performance, and DVH integrity are required before true clinical integration can be established.

Data availability statement

The original contributions presented in the study are included in the article/Supplementary Material, further inquiries can be directed to the corresponding author.

Ethics statement

The studies involving humans were approved by Istanbul Medipol University Non-Interventional Clinical Research Ethics Committee (Approval No:E-10840098-202.3.02-2932, Date: 09/05/2025). The studies were conducted in accordance with the local legislation and institutional requirements. Written informed consent for participation in this study was provided by the participants' legal guardians/next of kin.

Author contributions

MÇ: Conceptualization, Investigation, Methodology, Project administration, Supervision, Writing – original draft, Writing – review & editing. KE: Data curation, Writing – review & editing. MC: Writing – review & editing. IK: Data curation, Software, Visualization, Writing – review & editing. NK: Writing – review & editing. EM: Formal analysis, Writing – review & editing.

Funding

The author(s) declare that no financial support was received for the research and/or publication of this article.

Acknowledgments

The authors would like to thank the Department of Radiation Oncology at Bahçelievler Medipol Hospital for providing access to patient imaging data and supporting the clinical framework necessary for this study.

Conflict of interest

The authors declare that the research was conducted in the absence of any commercial or financial relationships that could be construed as a potential conflict of interest.

Generative AI statement

The author(s) declare that Generative AI was used in the creation of this manuscript. Generative AI (ChatGPT by OpenAI) was used to assist in language editing, grammar correction, and paraphrasing during the preparation of the manuscript and the cover letter. All scientific content, analyses, and interpretations were generated and verified solely by the authors, who take full responsibility for the integrity and accuracy of the work.

Any alternative text (alt text) provided alongside figures in this article has been generated by Frontiers with the support of artificial intelligence and reasonable efforts have been made to ensure accuracy, including review by the authors wherever possible. If you identify any issue please contact us.

Publisher's note

All claims expressed in this article are solely those of the authors and do not necessarily represent those of their affiliated organizations, or those of the publisher, the editors and the reviewers. Any product that may be evaluated in this article, or claim that may be made by its manufacturer, is not guaranteed or endorsed by the publisher.

Supplementary material

The Supplementary Material for this article can be found online at: https://www.frontiersin.org/articles/10.3389/fradi.2025. 1680803/full#supplementary-material

References

- 1. Boda-Heggemann J, Lohr F, Wenz F, Flentje M, Guckenberger M. kV cone-beam CT-based IGRT. Strahlenther Onkol. (2011) 187:284–91. doi: 10.1007/s00066-011-2236-4
- 2. Ríos I, Vásquez I, Cuervo E, Garzón Ó, Burbano J. Problems and solutions in IGRT for cervical cancer. *Rep Pract Oncol Radiother*. (2018) 23:517–27. doi: 10.1016/j.rpor.2018.05.002
- 3. Guckenberger M, Meyer J, Wilbert J, Baier K, Mueller G, Wulf J, et al. Conebeam CT based image-guidance for extracranial stereotactic radiotherapy of intrapulmonary tumors. *Acta Oncol (Madr)*. (2006) 45:897–906. doi: 10.1080/02841860600904839
- 4. Boda-Heggemann J, Walter C, Rahn A, Wertz H, Loeb I, Lohr F, et al. Repositioning accuracy of two different mask systems-3D revisited: comparison using true 3D/3D matching with cone-beam CT. *Int J Radiat Oncol Biol Phys.* (2006) 66:1568–75. doi: 10.1016/j.ijrobp.2006.08.054
- 5. Jaffray DA, Siewerdsen JH, Wong JW, Martinez AA. Flat-panel cone-beam computed tomography for image-guided radiation therapy. *Int J Radiat Oncol Biol Phys.* (2002) 53:1337–49. doi: 10.1016/S0360-3016(02)02884-5
- 6. Ouadah S, Jacobson M, Stayman JW, Ehtiati T, Weiss C, Siewerdsen JH. Correction of patient motion in cone-beam CT using 3D-2D registration. *Phys Med Biol.* (2017) 62:8813–31. doi: 10.1088/1361-6560/aa9254
- 7. Siewerdsen JH, Jaffray DA. Cone-beam computed tomography with a flat-panel imager: magnitude and effects of x-ray scatter. *Med Phys.* (2001) 28:220–31. doi: 10. 1118/1.1339879
- 8. de Koster RJC, Thummerer A, Scandurra D, Langendijk JA, Both S. Technical note: evaluation of deep learning based synthetic CTs clinical readiness for dose and NTCP driven head and neck adaptive proton therapy. *Med Phys.* (2023) 50:8023–33. doi: 10.1002/mp.16782
- 9. Okumus A, Durmus IF. Determination of tumor size and hounsfield unit/electron density values in three different ct scans for lung sbrt planning. UHOD Uluslar Hematol-Onkol Derg. (2021) 31:192–8. doi: 10.4999/uhod.214054
- 10. O'Connor LM, Choi JH, Dowling JA, Warren-Forward H, Martin J, Greer PB. Comparison of synthetic computed tomography generation methods, incorporating male and female anatomical differences, for magnetic resonance imaging-only definitive pelvic radiotherapy. *Front Oncol.* (2022) 12. doi: 10.3389/fonc.2022.822687
- 11. Oelfke U, Tücking T, Nill S, Seeber A, Hesse B, Huber P, et al. Linac-integrated kV-cone beam CT: technical features and first applications. *Med Dosim.* (2006) 31:62–70. doi: 10.1016/J.MEDDOS.2005.12.008
- 12. Gao L, Xie K, Wu X, Lu Z, Li C, Sun J, et al. Generating synthetic CT from low-dose cone-beam CT by using generative adversarial networks for adaptive radiotherapy. *Radiat Oncol.* (2021) 16. doi: 10.1186/s13014-021-01928-w
- 13. Rijken J, Jordan B, Crowe S, Kairn T, Trapp J. Improving accuracy for stereotactic body radiotherapy treatments of spinal metastases. *J Appl Clin Med Phys.* (2018) 19:453–62. doi: 10.1002/acm2.12395
- 14. Kazemifar S, Barragán Montero AM, Souris K, Rivas ST, Timmerman R, Park YK, et al. Dosimetric evaluation of synthetic CT generated with GANs for MRI-only proton therapy treatment planning of brain tumors. *J Appl Clin Med Phys.* (2020) 21:76–86. doi: 10.1002/acm2.12856
- 15. Chen L, Liang X, Shen C, Jiang S, Wang J. Synthetic CT generation from CBCT images via deep learning. *Med Phys.* (2020) 47:1115–25. doi: 10.1002/mp.13978
- 16. Altalib A, McGregor S, Li C, Perelli A. Synthetic CT image generation from CBCT: A Systematic Review. (2025).
- 17. Wongtrakool P, Puttanawarut C, Changkaew P, Piasanthia S, Earwong P, Stansook N, et al. Synthetic CT generation from CBCT and MRI using StarGAN in the pelvic region. *Radiat Oncol.* (2025) 20:18. doi: 10.1186/s13014-025-02590-2
- 18. Johnstone E, Wyatt JJ, Henry AM, Short SC, Sebag-Montefiore D, Murray L, et al. Systematic review of synthetic computed tomography generation

- methodologies for use in magnetic resonance imaging-only radiation therapy. *Int J Radiat Oncol Biol Phys.* (2018) 100:199-217. doi: 10.1016/j.ijrobp.2017.08.043
- 19. Farjam R, Nagar H, Kathy Zhou X, Ouellette D, Chiara Formenti S, DeWyngaert JK. Deep learning-based synthetic CT generation for MR-only radiotherapy of prostate cancer patients with 0.35 T MRI linear accelerator. J Appl Clin Med Phys. (2021) 22:93–104. doi: 10.1002/acm2.13327
- 20. Ryu K, Lee C, Han Y, Pang S, Kim YH, Choi C, et al. Multi-planar 2.5D U-net for image quality enhancement of dental cone-beam CT. *PLoS One.* (2023) 18. doi: 10.1371/journal.pone.0285608
- 21. Zhang Y, Yue N, Su MY, Liu B, Ding Y, Zhou Y, et al. Improving CBCT quality to CT level using deep learning with generative adversarial network. $Med\ Phys.\ (2021)\ 48:2816-26.\ doi: 10.1002/mp.14624$
- 22. Kida S, Nakamoto T, Nakano M, Nawa K, Haga A, Kotoku J, et al. Cone beam computed tomography image quality improvement using a deep convolutional neural network. *Cureus.* (2018) 10(4):e2548. doi: 10.7759/cureus.2548
- 23. Zhu W, Huang Y, Tang H, Qian Z, Du N, Fan W, et al. Anatomynet: deep 3D squeeze-and-excitation U-nets for fast and fully automated whole-volume anatomical segmentation. *BioRxiv.* (2018):392969. doi: 10.1101/392969
- 24. Liu Y, Lei Y, Wang T, Fu Y, Tang X, Curran WJ, et al. CBCT-based synthetic CT generation using deep-attention cycleGAN for pancreatic adaptive radiotherapy. *Med Phys.* (2020) 47:2472–83. doi: 10.1002/mp.14121
- 25. Heilemann G, Matthewman M, Kuess P, Goldner G, Widder J, Georg D, et al. Can generative adversarial networks help to overcome the limited data problem in segmentation? *Z Med Phys.* (2022) 32:361–8. doi: 10.1016/j.zemedi.2021.11.006
- 26. Fu L, Li X, Cai X, Miao D, Yao Y, Shen Y. Energy-guided diffusion model for CBCT-to-CT synthesis. *Comput Med Imaging Graph.* (2024) 113. doi: 10.1016/j.compmedimag.2024.102344
- 27. Zhang Y, Li L, Wang J, Yang X, Zhou H, He J, et al. Texture-preserving diffusion model for CBCT-to-CT synthesis. *Med Image Anal.* (2025) 99. doi: 10. 1016/j.media.2024.103362
- 28. Kazerouni A, Aghdam EK, Heidari M, Azad R, Fayyaz M, Hacihaliloglu I, et al. Diffusion models in medical imaging: a comprehensive survey. *Med Image Anal.* (2023) 88. doi: 10.1016/j.media.2023.102846
- 29. Chen X, Liu Y, Yang B, Zhu J, Yuan S, Xie X, et al. A more effective CT synthesizer using transformers for cone-beam CT-guided adaptive radiotherapy. *Front Oncol.* (2022) 12. doi: 10.3389/fonc.2022.988800
- 30. Huijben EMC, Terpstra ML, Galapon AJ, Pai S, Thummerer A, Koopmans P, et al. Generating synthetic computed tomography for radiotherapy: synthRAD2023 challenge report. *Med Image Anal.* (2024) 97. doi: 10.1016/j.media.2024.103276
- 31. Koike Y, Takegawa H, Anetai Y, Nakamura S, Yoshida K, Yoshida A, et al. Cone-Beam CT to CT image translation using a transformer-based deep learning model for prostate cancer adaptive radiotherapy. *J Imaging Inform Med.* (2025) 38:2490–99. doi: 10.1007/s10278-024-01312-6
- 32. Ronneberger O, Fischer P, Brox T. U-net: Convolutional Networks for Biomedical Image Segmentation. Lecture Notes in Computer Science (including Subseries Lecture Notes in Artificial Intelligence and Lecture Notes in Bioinformatics). Cham: Springer Verlag (2015). p. 234–41. doi: 10.1007/978-3-319-24574-4_28
- 33. Maspero M, Bentvelzen LG, Savenije MHF, Guerreiro F, Seravalli E, Janssens GO, et al. Deep learning-based synthetic CT generation for paediatric brain MR-only photon and proton radiotherapy. *Radiother Oncol.* (2020) 153:197–204. doi: 10.1016/j.radonc.2020.09.029
- 34. Yoganathan SA, Aouadi S, Ahmed S, Paloor S, Torfeh T, Al-Hammadi N, et al. Generating synthetic images from cone beam computed tomography using self-attention residual UNet for head and neck radiotherapy. *Phys Imaging Radiat Oncol.* (2023) 28. doi: 10.1016/j.phro.2023.100512